CHALMERS
UNIVERSITY OF TECHNOLOGY

Mode Sensitivity Analysis of Subwavelength Grating Slot Waveguides

Citation for the original published paper (version of record):
Odeh, M., Twayana, K., Sloyan, K. et al (2019). Mode Sensitivity Analysis of Subwavelength Grating Slot Waveguides. IEEE Photonics Journal, 11(5).
http://dx.doi.org/10.1109/JPHOT.2019.2939088

(article starts on next page)

IEEE Photonics Journal
An IEEE Photonics Society Publication

Open Access

Mode Sensitivity Analysis of Subwavelength Grating Slot Waveguides

Volume 11, Number 5, October 2019

Mutasem Odeh
Krishna Twayana
Karen Sloyan
Juan E. Villegas
Sujith Chandran
Marcus S. Dahlem

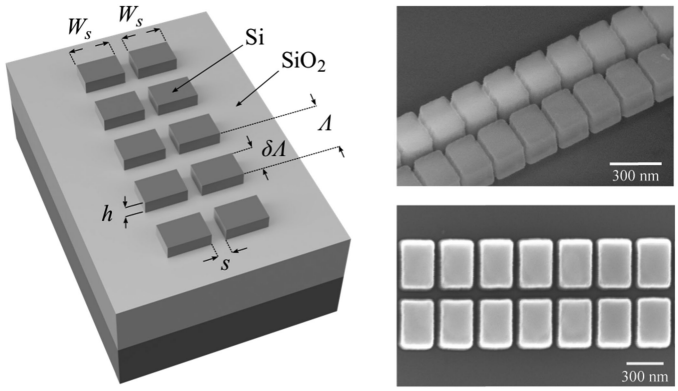

DOI: 10.1109/JPHOT.2019.2939088

IEEE photonics SOCIETY
IEEE

Mode Sensitivity Analysis of Subwavelength Grating Slot Waveguides

Mutasem Odeh,[1,2] **Krishna Twayana**,[1,3] **Karen Sloyan**,[1] **Juan E. Villegas**,[1,4] **Sujith Chandran**,[1] **and Marcus S. Dahlem**[1,5]

[1]Electrical and Computer Engineering Department, Khalifa University of Science and Technology, Abu Dhabi, United Arab Emirates
[2]Department of Electrical Engineering and Computer Sciences, University of California, Berkeley, CA 94720 USA
[3]Department of Microtechnology and Nanoscience, Chalmers University of Technology, Gothenburg 412 96, Sweden
[4]Electrical and Computer Engineering Department, New York University, Abu Dhabi, United Arab Emirates
[5]Interuniversity Microelectronics Center, Leuven 3001, Belgium

DOI:10.1109/JPHOT.2019.2939088

Manuscript received August 2, 2019; accepted August 28, 2019. Date of publication September 2, 2019; date of current version September 20, 2019. All fabrication and characterization was performed at Khalifa University. The work was supported by Khalifa University/SRC Center of Excellence on Integrated Photonics award number 8434000185, and Khalifa University award number 8474000100. Corresponding author: Sujith Chandran (e-mail: sujith.chandran@ku.ac.ae).

Abstract: In this paper, we investigate the mode sensitivity (S_{mode}) of subwavelength grating slot (SWGS) waveguides. S_{mode} is an important parameter in various waveguide-based photonic circuits such as sensors, modulators, and thermally-controlled devices. It is a measure of the sensitivity of the waveguide effective index towards the refractive index perturbations in the cladding medium. The SWGS waveguide exhibits high mode sensitivity, as it combines sensitivity enhancement features of both slot and subwavelength grating waveguides. Finite-difference time-domain simulations are performed for the analysis, design, and optimization of the hybrid structure. The SWGS waveguide is incorporated into a Mach-Zehnder interferometer and fabricated on a silicon-on-insulator platform for the experimental estimation of S_{mode}. The measured S_{mode} value of 79% is consistent with the theoretical prediction of 83%.

Index Terms: Subwavelength grating, slot waveguide, silicon-on-insulator, integrated optics, sensor.

1. Introduction

Segmenting waveguide structures at the subwavelength scale of the propagating light is an elegant and flexible method to tailor the dispersion and nonlinear properties of photonic devices without modifying the material composition. Diffraction effects of the periodic structure are eliminated when the periodicity scale is in the subwavelength regime, where the waveguide can be modeled as a homogeneous optical medium with an effective refractive index that depends on the dimensions and geometry of its constituent materials. This method has been employed in early studies of electromagnetic polarizations at the radio wave spectrum [1], and later to realize anti-reflective surfaces in the visible range [2]. The unique advantages of this method have been remarkably unfolded in integrated silicon photonic devices, as it has been applied in fiber-to-chip grating couplers to minimize mode mismatch losses [3], in multiplexers to widen the operational bandwidth [4], and

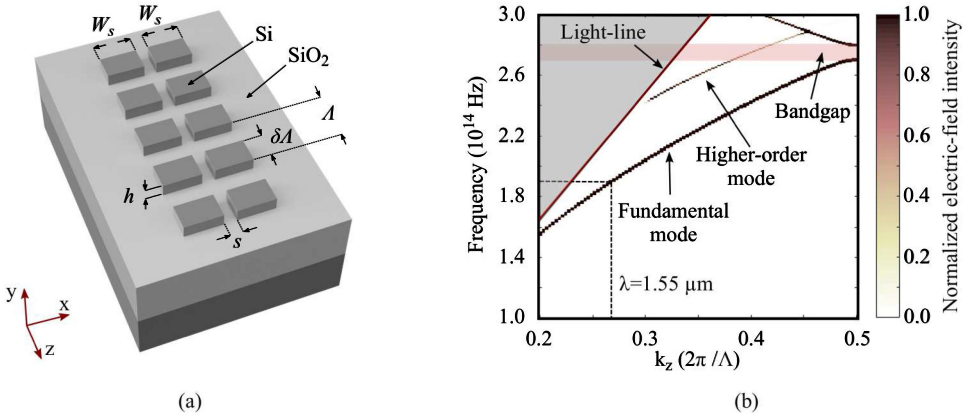

Fig. 1. SWGS waveguide: (a) schematic view of the structure on an SOI substrate, and (b) photonic band diagram (TE polarization) for a waveguide with $h = 220$ nm, $W_s = 300$ nm, $s = 80$ nm, $\Lambda = 260$ nm, $\delta = 75\%$, and cladding index $n_c = 1.3$. The photonic bandgap region for the fundamental mode is indicated in red.

in multi-mode interference couplers to mitigate the wavelength dependence [5]. This method has also been used to reduce the propagation loss of subwavelength grating (SWG) waveguides by relaxing the modal confinement [6], and has promoted this type of waveguides to be used in sensors [7]–[10], modulators [11], and athermal devices [12].

SWG structures have recently been modified as slotted SWGs for delocalizing the guided mode profile further from the silicon core in order to suppress non-linear optic effects [13], [14]. Moreover, the weak modal confinement of the subwavelength grating slot (SWGS) waveguide has been used for sensing applications [15], [16]. Both are enabled by the high dependence of the waveguide effective index on the cladding material, which is quantified by the *mode sensitivity* (S_{mode}) parameter. As we identify SWGS waveguides as important components to be used in many integrated photonic circuits, we here present a complete study of their mode sensitivity, which has previously been studied for different waveguide structures [17]–[19].

In this study, we estimate S_{mode} using 3D finite-difference time-domain (FDTD) simulations. Additionally, we show that S_{mode} is directly related the overlap integral. This treatment is expected to provide a qualitative understanding that will allow to control the effective index of the SWGS waveguide by engineering the cladding material composition and geometry. In Section 2 we examine the dispersion characteristics of the SWGS waveguide, and in Section 3 we optimize the structure to maximize S_{mode} within the fabrication constrains. In Section 4, we present the design aspects of a Mach-Zehnder interferometer (MZI) for the experimental extraction of S_{mode}. Fabrication and characterization details are given in Section 5, following with a discussion on the obtained results. Finally, conclusions and future scope of the study are briefly outlined in Section 6.

2. Waveguide Structure and Band Diagram

An SWGS waveguide is a periodically segmented slot waveguide, as schematically shown in Fig. 1(a). A single period (Λ) consists of two silicon segments of equal width (W_s) and length ($\delta\Lambda$), where δ is the duty cycle, separated by a slot width (s), and by a cladding section of length $(1-\delta)\Lambda$. In order to operate the grating structure in the subwavelength regime, Λ must be smaller than $\lambda/2n_{eff}$ to prevent Bragg reflection and diffraction [1], where λ is the free-space wavelength and n_{eff} the mode effective index. However, the dimensions (periodicity and section lengths) need to be large enough to realize the structure within the fabrication constrains. The structure is designed on a silicon-on-insulator (SOI) platform with a 220 nm-thick top silicon layer (h) and 3 μm-thick buried oxide (BOX) layer. Photonic bandgap calculations are performed using 3D FDTD simulations for the transverse electric (TE) polarization. Fig. 1(b) shows the photonic band diagram for an SWGS

waveguide with $\Lambda = 260$ nm, $W_s = 300$ nm, $s = 80$ nm, $\delta = 75\%$, and $h = 220$ nm. The background refractive index for the simulation is set to 1.3, which closely represents the refractive index of typical fluid claddings. The color scale in the dispersion curves (for fundamental and first higher order modes) indicates the relative intensity of the electric field inside the waveguide structure, which is inversely proportional to the propagation loss of the corresponding mode. The photonic bandgap region of the fundamental mode is indicated in the band structure. As seen from the figure, the wavelength of interest ($\lambda \sim 1550$ nm) lies in the subwavelength regime, as it is located well below the photonic bandgap region. In this regime, the propagating mode is lossless, as indicated by the near unity normalized electric field intensity. The SWGS structure was designed to obtain single mode operation with high sensitivity to the waveguide cladding, while satisfying the minimum feature size limitations imposed by our fabrication constrains (~40 nm gap size using electron-beam lithography and reactive-ion etching).

3. Mode Sensitivity Analysis

In this study, S_{mode} of the waveguide is defined as the rate of change of the fundamental mode effective index (n_{eff}) with respect to the refractive index of the cladding medium (n_c), as given by the following equation:

$$S_{mode} = \frac{\partial n_{eff}}{\partial n_c}. \tag{1}$$

In general, high S_{mode} over a wide range of n_c is preferred for many applications. For example, it corresponds to higher sensitivity in photonic sensors; a higher n_{eff} change due to a cladding index perturbation translates into a higher spectral shift in wavelength-based detection sensors [15] or higher absorption in intensity detection sensors [20]. In the case of electro-optic modulators, higher S_{mode} facilitates faster switching with low power consumption [11]. However, when engineering athermal waveguides by combining opposite thermo-optic coefficient materials [12], S_{mode} needs to be precisely controlled and must be designed to be tolerant to dimensional variations in the fabrication process. Therefore it is important to understand and optimize the various mechanisms that contribute to S_{mode} in SWGS waveguides. S_{mode} can be directly estimated from the dispersion diagrams corresponding to different cladding refractive index values. It is also known that S_{mode} can be related to the overlap integral in the cladding (Γ_c) [8], [9]. This approach helps identifying the contribution of each of the waveguide geometrical parameters to S_{mode}. In this work, Γ_c is expressed as the sum of the overlap factors of the following three subregions: (i) the slot region between two silicon segments (Γ_{slot}) with a volume of $s \times \delta\Lambda \times h$; (ii) the gap region between the periodic silicon segments (Γ_{gap}) with a volume of $(2W_s + s) \times (1 - \delta)\Lambda \times h$; and (iii) the remaining top cladding medium (Γ_{top}). For the SWGS waveguide, the electric field intensity varies periodically along the propagation direction. Consequently, Γ_i can be calculated by integrating the intensity over the volume of subregion i (*slot*, *gap*, *top*) in a single unit cell volume (a) with a period of Λ, as given by Eq. 2 [19]:

$$\Gamma_c = \Gamma_{slot} + \Gamma_{gap} + \Gamma_{top}, \qquad \Gamma_i = \frac{\iiint_i |E(x, y, z)|^2 \, dx \, dy \, dz}{\iiint_a |E(x, y, z)|^2 \, dx \, dy \, dz}. \tag{2}$$

Γ_{slot} can mainly be maximized by optimizing the slot-waveguide aspect of the SWGS structure. The discontinuity of the normal component of the electric field (E_x) between the high contrast refractive index media with a slot width comparable to the evanescent field decay length will lead to an enhanced and confined electric field in the cladding slot region, as shown Fig. 2(a). A similar argument can be applied to the E_z component and the periodic gap region in order to increase Γ_{gap}, as seen in Fig. 2(b). Lastly, Γ_{top} is increased by reducing the effective refractive index via mode delocalization (decrease δ) [21]. A careful and simultaneous optimization of the three mechanisms leads to a weak mode confinement in the core medium and high mode overlap with the cladding medium. It should be noted that the enhancement of the E_x and E_z components in the slot and gap regions directly contributes to the improvement of S_{mode}, as most of the electric field is localized in

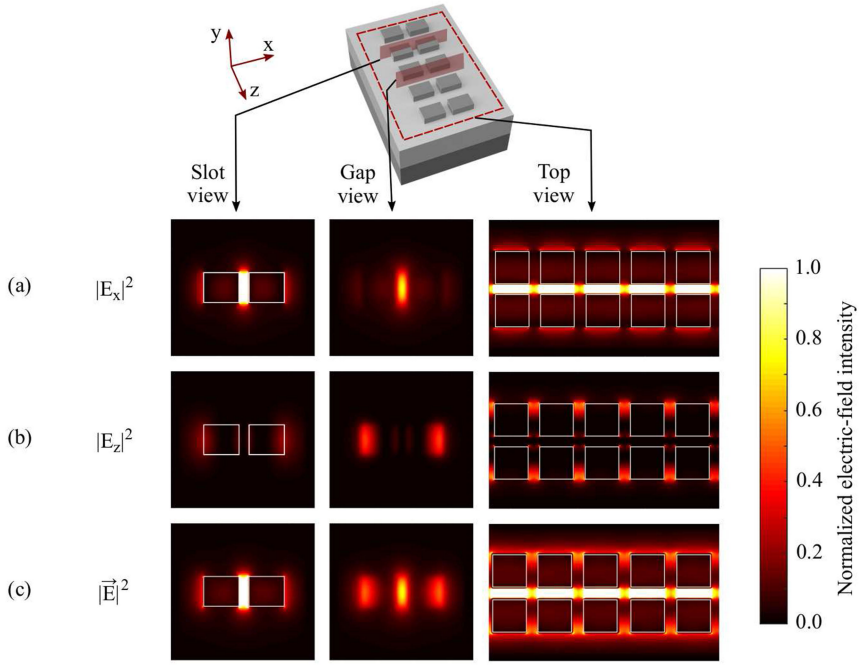

Fig. 2. Normalized electric field intensity profile (TE polarization) shown at various cross-sections of the SWGS structure, simulated for $\lambda = 1550$ nm and $n_c = 1.3$: (a) $|Ex|^2$, (b) $|E_z|^2$, and (c) the total electric field intensity ($|\vec{E}|^2$). The slot view is taken at the middle of the periodic silicon segments, the gap view in between the periodic silicon segments, and the top view at the middle of the silicon device layer.

the cladding medium. However, only a part of the delocalized electric field (by the reduction of δ) contributes to the improvement of S_{mode}, while the remaining part extends into the unperturbed BOX layer. The net effect of these three mechanisms results in high mode overlap in the slot and gap regions, and mode delocalization in the waveguide surrounding, as shown in Fig. 2(c).

The mode sensitivity simulation is performed by calculating the effective index of the waveguide mode using 3D FDTD simulations (Lumerical FDTD). A non-uniform meshing with minimum step size of 10 nm is used for all simulations, which proved to be a good compromise between accuracy and computational efficiency. Perfectly matched layer (PML) simulation boundaries along the x and y axes are set 3 μm apart from the center of the waveguide. Periodic boundary conditions are applied along the z axis, with a separation distance Λ and a phase shift $\Phi = k_z\Lambda$ between two consecutive planes. The structure is simulated with a mode source that lunches the fundamental TE mode of the slot cross-section in the waveguide, which is the closest and computationally more efficient source to excite the fundamental TE mode of the SWGS waveguide. Additional convergence tests were performed using a finer mesh size with dipole sources placed randomly across the simulation region to excite all the possible supported modes. The supported wavelength (λ_r) is determined from the Fourier Transform of the time-domain monitors that are placed randomly inside the simulation region. A binary search algorithm was then implemented to find the value of Φ that results in $\lambda_r = 1550$ nm, which leads to the estimation of n_{eff}. The simulation is repeated for 20 points of n_c between 1.3 to 1.4. The resulting n_{eff} vs. n_c data is fitted using a first-order polynomial to extract the value of S_{mode} for a specific set of parameters of the SWGS structure. The same simulation is also used to calculate Γ_i using frequency-domain field monitors. An iterative optimization was performed manually, and the optimized structural parameters for $h = 220$ nm and $\Lambda = 260$ nm were found to be $W_s = 300$ nm, $s = 80$ nm, and $\delta = 75\%$, resulting in $S_{mode} = 83\%$ with $n_{eff} \sim 1.67$ and $n_g \sim 2.56$. It should be noted that perturbation theory can also be used to effectively estimate the mode sensitivity, as done for other waveguide geometries [17].

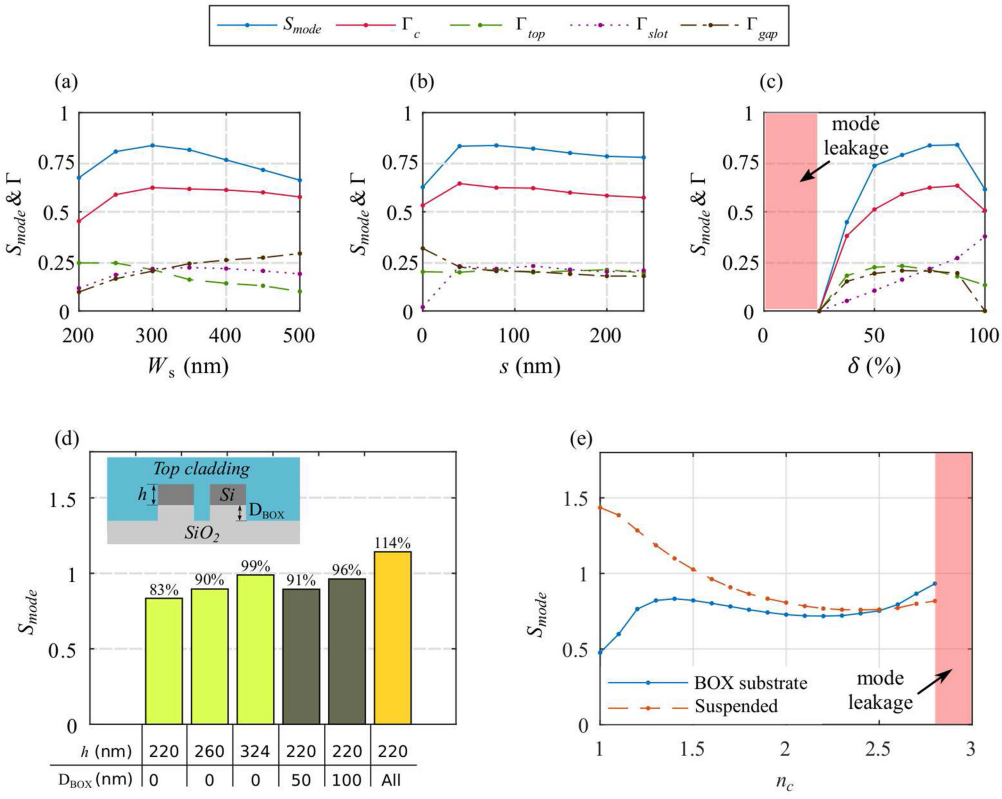

Fig. 3. Mode sensitivity analysis: dependency of S_{mode} and mode-overlap factor (Γ) on (a) width of the silicon segments, for $s = 80$ nm and $\delta = 75\%$, (b) slot width, for $W_s = 300$ nm and $\delta = 75\%$, and (c) duty cycle, for $W_s = 300$ nm and $s = 80$ nm; (d) S_{mode} calculated for various device layer heights and BOX etch depths (schematic cross-section view of the SWGS shown in the inset), where the last yellow bar corresponds to complete BOX layer removal and a suspended structure; (e) S_{mode} as a function of the cladding index (n_c) for supported and suspended structures.

To understand the effect of the waveguide structural parameters on the mode sensitivity, they have been deviated individually from the optimal design while monitoring the overlap factors and the corresponding S_{mode}. As seen in Fig. 3(a), increasing W_s increases n_{eff} which consequently reduces Γ_{top} due to better mode confinement in the silicon segments. Simultaneously, the total volume of the gap region increases, enhancing Γ_{gap}. However, Γ_{slot} stabilizes around $W_s = 350$ nm, dictated by the optimum evanescent field extension in the slot region. On the other hand, the structure shows a good tolerance for $s = 30$ to 240 nm, as shown in Fig. 3(b). This can be attributed to the volume compensation with the reduced electric field enhancement as s increases. The same effect is observed for Γ_{gap} while varying δ between 50 to 75%, as shown in Fig. 3(c). However, it can be seen that S_{mode} drops to zero for $\delta < 25\%$, due to the extreme mode delocalization. Results from Figs. 3(a)–(c) confirm that Γ_c and S_{mode} are directly related, as both the parameters exhibit similar dependency on the geometrical parameters W_s, s and δ. Although the SWGS structure is designed on an SOI platform with 220 nm-thick device layer, we observe a significant enhancement of S_{mode} for slightly thicker device layers, confirming a recent investigation carried out in SWG waveguides [22]. Fig. 3(d) compares the S_{mode} for $h = 220$ nm, 260 nm and 324 nm. The enhancement of S_{mode} with respect to the device layer height is achieved due to the mode elevation (mode profile shifts away from the BOX layer, hence a better interaction with the cladding) which, in turn, increases Γ_{slot} and Γ_{gap}. This implies that similar enhancement can be achieved if the BOX layer is etched in addition to the silicon layer. Fig. 3(d) shows the impact of BOX layer removal. For, $h = 220$ nm, an anisotropic BOX etch profile of 50 nm and 100 nm depth results in S_{mode} of 91% and 96%, respectively. The

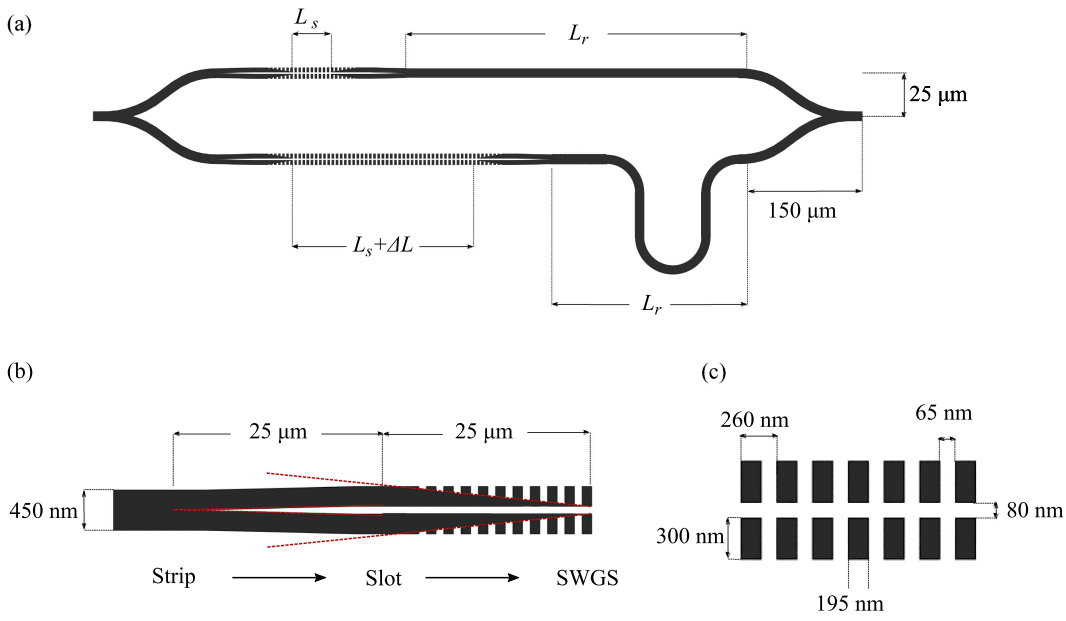

Fig. 4. Schematic representation of the MZI used to estimate S_{mode} for the SWGS waveguide: (a) MZI configuration, (b) strip-to-SWGS linear taper with red dashed lines indicating the linear transitions, and (c) optimized SWGS parameters.

inset shows the cross-section view of the SWGS with the anisotropic etch profile of the BOX layer. The maximum attainable S_{mode} for the optimized dimensions is 114%, which occurs when both upper and lower claddings contribute to perturb n_{eff} (suspended structure). Recent work on SWG waveguides has shown a similar sensitivity enhancement by pedestaling the nanostructures by an additional wet-etch processing step [23]. Fig. 3(e) shows the S_{mode} calculated over a wide cladding refractive index (n_c) range, for both supported (with BOX) and suspended (without BOX) SWGS structures. As can be seen in the figure, the supported SWGS has a drop in S_{mode} for low n_c values (1.0 to 1.3) due to the high mode overlap with the supporting substrate, while in the suspended version it increases up to almost 150%. On the other hand, the roles are switched at high n_c values ($\sim$2.5), and both modes start to leak beyond $n_c = 2.8$.

4. Mode Sensitivity Estimation

An asymmetric Mach-Zehnder interferometer (MZI) is used for the experimental extraction of S_{mode}. Fig. 4(a) shows the schematic layout of the asymmetric MZI with different lengths of SWGS waveguides in each of the arms. Straight and curved waveguide segments of 20 μm radius are added to one of the arms of the MZI to equalize the length of the reference strip waveguides ($height = 220$ nm, $width = 450$ nm) in both arms. The reference strip waveguide length (L_r) is fixed to 170 μm to ensure minimum loss in the waveguide bends. This enables us to directly relate the free spectral range of the MZI to the length difference (ΔL) between the two SWGS waveguides in the different arms. In order to efficiently couple the mode between the strip and the SWGS waveguides, we use two separate 25 μm-long linear adiabatic tapers. The first taper linearly transforms the strip waveguide into a slot waveguide, while the second taper smoothly engraves the subwavelength grating features on the outer sides of the slot structure. The schematic top view of the strip-to-SWGS mode converter is shown in Fig. 4(b), with the linear transitions indicated with red dashed lines. The strip-to-SWGS mode converter was not optimized, as it is not critical to estimate the mode sensitivity of the SWGS waveguide. The phase difference between the two Mach-Zehnder arms is proportional to the effective optical path length difference. Since the MZI is balanced, except in its

SWGS section, the phase difference can be expressed as

$$\Delta\phi = \frac{2\pi}{\lambda}\left(\Delta L\,.n_{eff}^{SWGS}\right). \tag{3}$$

Consequently, any wavelength shift introduced in the MZI can be exclusively attributed to the effective index change of the SWGS waveguide (n_{eff}^{SWGS}) over the length ΔL. From Eq. (3), the MZI sensitivity (S_{MZI}) and the free spectral range (FSR) can be derived as

$$S_{MZI} = \frac{\partial\lambda}{\partial n_c} = \frac{\lambda\,\frac{\partial n_{eff}^{SWGS}}{\partial n_c}}{n_g^{SWGS}}, \tag{4}$$

$$FSR = \frac{\lambda^2}{\Delta L\,\times n_g^{SWGS}}. \tag{5}$$

From Eqs. (4) and (5), S_{mode} can be expressed as

$$S_{mode} = \frac{\partial n_{eff}^{SWGS}}{\partial n_c} = \frac{\lambda \times S_{MZI}}{\Delta L\,\times FSR}. \tag{6}$$

Therefore, S_{mode} can be experimentally extracted by measuring the MZI sensitivity (S_{MZI}) and its FSR at the desired wavelength. Using the simulated values of S_{mode} (83%) and n_g (2.56), the MZI sensitivity is calculated to be 502 nm/RIU at a wavelength of 1550 nm. The important design parameter of the MZI is ΔL, which should be chosen to ensure a detectable spectral shift ($\Delta\lambda < FSR$). The n_c values used in the subsequent sensing experiments differ by a maximum of 0.015 RIU, which corresponds to a $\Delta\lambda \sim 7.5$ nm shift in the MZI spectral response. Consequently, we have safely chosen ΔL as 90 μm, which corresponds to an FSR of 10.5 nm.

5. Fabrication and Characterization

The optimized design was fabricated on an SOI stack ($h = 220$ nm and 3 μm-thick BOX) using electron-beam lithography and inductively coupled plasma (ICP) reactive-ion etching. To ensure high resolution patterning, hydrogen silsesquioxane (HSQ), a negative tone resist, was exposed at a 25 keV beam energy and a dose of 3500 μC/cm^2. Following the e-beam exposure, an undiluted AZ 400 K solution was used to develop the pattern. The resist pattern was then transferred to the silicon device layer using fluorine-based reactive-ion etching (gas flow rate: SF_6:CH_4::25 sccm: 25 sccm, forward power: 10 W, ICP power: 800 W). This fabrication procedure allowed us to reliably produce features with smooth and vertical sidewall profiles down to 40 nm. Finally, a diluted hydrofluoric (HF) acid solution (HF:DI water::1:10) was used to remove the HSQ resist completely. This step ensures the exposure of the full device layer to the top cladding, facilitating subsequent sensing experiments. Fig. 5(a) shows the optical microscope image of the fabricated MZI structure. An on-chip low-loss TE-pass polarizer [24] was used at the output section of the MZI to eliminate any unintentionally excited TM polarization. SEM images of the important sections of the MZI are shown in Figs. 5(b)–(e). A lensed fiber was used to couple light from a tunable laser source (1530 to 1570 nm) at the cleaved end-facet of the chip. The output signal (from the chip) was collected by another lensed fiber and fed into a photodetector to record the transmission spectrum. In order to ensure that only TE polarized light was coupled into the device, an off-chip polarization controller was used between the laser source and the input lensed fiber.

The normalized MZI transmission spectrum for $n_c = 1.315$ is shown in Fig. 6(a). The FSR is estimated to be 13 nm, which is larger than the one obtained in simulation (10.5 nm). The difference in FSR is likely attributed to a small imbalance in the strip waveguide optical lengths in the MZI arms, due to a combination of the following: (i) slight variation in the device layer thickness and/or waveguide width; (ii) waveguide bends in the strip section of the bottom arm of the MZI that extend into an additional EBL writing field (with two additional stitching errors); and (iii) unequal effective index in the bent and straight waveguide sections. This is especially pronounced due to the high

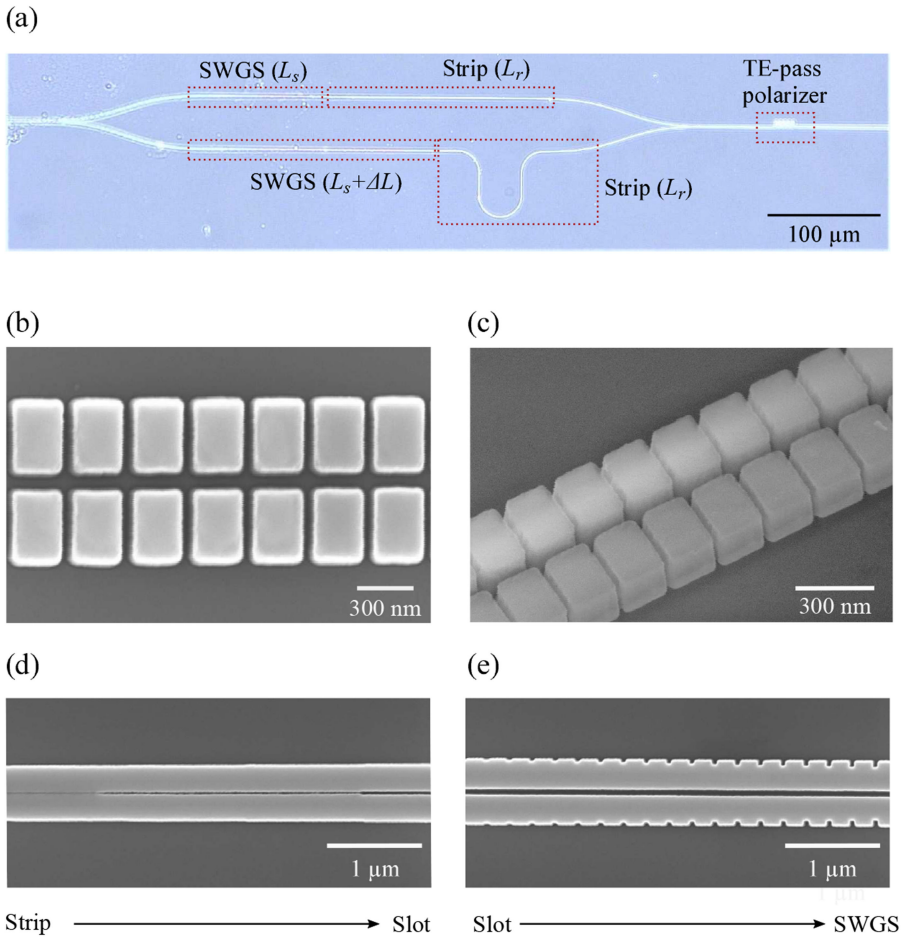

Fig. 5. Fabricated SWGS structure on an SOI platform: (a) optical image of the MZI device with an on-chip TE-pass polarizer at the output, (b) top SEM view showing a well defined SWGS structure, (c) perspective SEM view showing vertical and smooth sidewalls, (d) top SEM view of the taper section used to convert the strip waveguide mode into the slot waveguide mode, and (e) top SEM view of the taper section used to convert the slot waveguide mode into the SWGS waveguide mode.

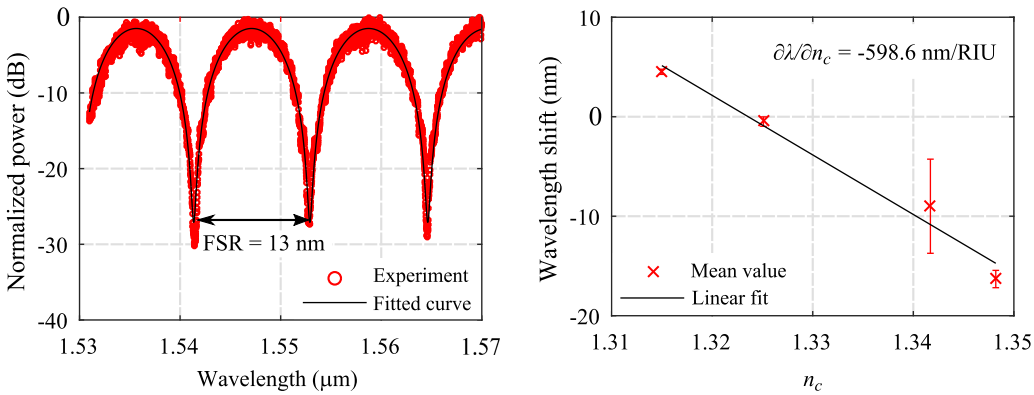

Fig. 6. MZI characterization: (a) normalized MZI transmission spectrum for $n_c = 1.315$, and (b) shift of MZI wavelength response, around $\lambda = 1550$ nm, for 4 different IPA-water solutions.

group index of the strip waveguide ($n_g^{strip} \simeq 4$). However, this mismatch has little effect on the estimation of S_{mode} due to the high mode confinement and low sensitivity of the strip waveguide. Therefore, our assumptions used in deriving Eq. (6) are still valid. In order to estimate S_{MZI}, the transmission spectrum was measured for 4 different concentrations of an isopropanol (IPA) aqueous solution. The corresponding average spectral shifts of the minima at wavelengths around 1550 nm, for each IPA-water concentration, are plotted in Fig. 6(b), and result in an S_{MZI} value of -598.6 nm/RIU. Each data point in the plot is obtained by averaging the results of 5 independent measurement cycles between the 4 IPA-water concentrations. Using Eq. (6), S_{mode} of the fabricated SWGS waveguide is estimated to be 79%, which is in good agreement with the 83% sensitivity obtained from numerical simulations.

6. Conclusions

We present a detailed analysis on the SWGS mode sensitivity (change in the effective index as a function of the cladding refractive index perturbations). The critical geometrical parameters affecting the strength of S_{mode} are optimized for the structure, taking into account the fabrication limitations. The optimum design offers high S_{mode} with relaxed fabrication requirements. An asymmetric Mach-Zehnder interferometer configuration is used for the experimental extraction of S_{mode}. The experimental (79%) and designed (83%) values of S_{mode} are in good agreement. Further improvement of the device sensitivity can be achieved by increasing the device layer height of the SOI stack and/or by deeply etching the BOX layer anisotropically. Due to its high sensitivity, the SWGS waveguide is suitable for integrated sensing applications, electro-optic modulators and athermal photonic devices.

References

[1] R. Halir *et al.*, "Waveguide sub-wavelength structures: A review of principles and applications," *Laser Photon. Rev.*, vol. 9, no. 1, pp. 25–49, 2015.

[2] P. B. Clapham and M. C. Hutley, "Reduction of lens reflexion by the "Moth Eye" principle," *Nature*, vol. 244, pp. 281–282, 1973.

[3] P. Cheben, D.-X. Xu, S. Janz, and A. Densmore, "Subwavelength waveguide grating for mode conversion and light coupling in integrated optics," *Opt. Exp.*, vol. 14, no. 11, pp. 4695–4702, 2006.

[4] P. Cheben *et al.*, "Refractive index engineering with subwavelength gratings for efficient microphotonic couplers and planar waveguide multiplexers," *Opt. Lett.*, vol. 35, no. 15, pp. 2526–2528, 2010.

[5] A. Maese-Novo *et al.*, "Wavelength independent multimode interference coupler," *Opt. Exp.*, vol. 21, no. 6, pp. 7033–7040, 2013.

[6] P. J. Bock *et al.*, "Subwavelength grating periodic structures in silicon-on-insulator: a new type of microphotonic waveguide," *Opt. Exp.*, vol. 18, no. 19, pp. 20251–20262, 2010.

[7] J. G. Wanguemert-Perez *et al.*, "Evanescent field waveguide sensing with subwavelength grating structures in silicon-on-insulator," *Opt. Lett.*, vol. 39, no. 15, pp. 4442–4445, 2014.

[8] J. Flueckiger *et al.*, "Sub-wavelength grating for enhanced ring resonator biosensor," *Opt. Exp.*, vol. 24, no. 14, pp. 15672–15686, 2016.

[9] H. Yan *et al.*, "Unique surface sensing property and enhanced sensitivity in microring resonator biosensors based on subwavelength grating waveguides," *Opt. Exp.*, vol. 24, no. 26, pp. 29724–29733, 2016.

[10] L. Huang *et al.*, "Improving the detection limit for on-chip photonic sensors based on subwavelength grating racetrack resonators," *Opt. Exp.*, vol. 25, no. 9, pp. 10527–10535, 2017.

[11] H. Yan *et al.*, "One-dimensional photonic crystal slot waveguide for silicon-organic hybrid electro-optic modulators," *Opt. Lett.*, vol. 41, no. 23, pp. 5466–5469, 2016.

[12] M. Ibrahim *et al.*, "Athermal silicon waveguides with bridged subwavelength gratings for TE and TM polarizations," *Opt. Exp.*, vol. 20, no. 16, pp. 18356–18361, 2012.

[13] Z. Ruan, L. Shen, S. Zheng, and J. Wang, "Subwavelength grating slot (SWGS) waveguide on silicon platform," *Opt. Exp.*, vol. 25, no. 15, pp. 18250–18264, 2017.

[14] Z. Ruan *et al.*, "Subwavelength grating slot (SWGS) waveguide at 2 μm for chip-scale data transmission," *Nanophotonics*, vol. 7, no. 5, pp. 865–871, 2018.

[15] E. Luan *et al.*, "Enhanced sensitivity of subwavelength multibox waveguide microring resonator label-free biosensors," *IEEE J. Sel. Topics Quantum Electron.*, vol. 25, no. 3, pp. 1–11, May/Jun. 2019.

[16] M. Odeh, K. Twayana, K. Sloyan, J. E. Villegas, S. Chandran, and M. S. Dahlem, "Slotted subwavelength grating waveguides for compact optofluidic sensors," in *Proc. Int. Conf. Opt. MEMS Nanophoton.*, Lausanne, Switzerland, 2018, pp. 1–2.

[17] D. M. Kita, J. Michon, S. G. Johnson, and J. Hu, "Are slot and sub-wavelength grating waveguides better than strip waveguides for sensing?," *Optica*, vol. 5, no. 9, pp. 1046–1054, 2018.
[18] S. TalebiFard *et al.*, "Optimized sensitivity of Silicon-on-Insulator (SOI) strip waveguide resonator sensor," *Biomed. Opt. Exp.*, vol. 8, no. 2, pp. 500–511, 2017.
[19] F. Dell'Olio and V. M. N. Passaro, "Optical sensing by optimized silicon slot waveguides," *Opt. Exp.*, vol. 15, no. 8, pp. 4977–4993, 2007.
[20] V. M. Lavchiev *et al.*, "Silicon photonics in the mid-infrared: waveguide absorption sensors," *Proc. IEEE SENSORS*, Valencia, Spain, pp. 645–648, 2014.
[21] S. M. Rytov, "Electromagnetic properties of a finely stratified medium," *Sov. Phys. J. Exp. Theor. Phys.*, vol. 2, no. 3, pp. 466–475, 1956.
[22] J. G. Wanguemert-Perez *et al.*, "Subwavelength structures for silicon photonics biosensing," *Opt. Laser Technol.*, vol. 109, pp. 437–448, 2019.
[23] C.-W. Chang *et al.*, "Pedestal subwavelength grating metamaterial waveguide ring resonator for ultra-sensitive label-free biosensing," *Biosensors Bioelectron.*, vol. 141, 2019, Art. no. 111396.
[24] H. Zafar, P. Moreira, A. M. Taha, B. Paredes, M. S. Dahlem, and A. Khilo, "Compact silicon TE-pass polarizer using adiabatically-bent fully-etched waveguides," *Opt. Exp.*, vol. 26, no. 24, pp. 31850–31860, 2018.